Measurement of the HD($v'=2,J'=3$) product differential cross section for the H+D_2 exchange reaction at 1.55±0.05 eV using the photoloc technique

Félix Fernández-Alonso, Brian D. Bean, and Richard N. Zare[a)]
Department of Chemistry, Stanford University, Stanford, California 94305

(Received 19 January 1999; accepted 30 March 1999)

We describe a time-of-flight apparatus that uses core extraction to determine nascent product laboratory velocity distributions from which differential cross sections may be deduced. We emphasize the characterization of the instrument, the reaction conditions, and the calibration procedure. For this purpose, we have measured H-atom velocity distributions from HBr photolysis, as well as the $H_2(v'=4,J'=1)$ velocity distribution arising from the H+HBr reaction under quasi-monoenergetic collision conditions at 1.9 eV. Collisional energy spread and reagent internal state distributions were determined from the rotational and translational temperatures of the HBr photolytic precursor and the D_2 diatomic reagent. The differential cross section for H+D_2 →HD($v'=2,J'=3$)+D at 1.55±0.05 eV is presented and found to peak near 145°±10° with an approximate full width at half maximum (FWHM) of 40°. © *1999 American Institute of Physics.* [S0021-9606(99)00724-2]

I. INTRODUCTION

Since the early theoretical work on the H_3 potential energy surface by London,[1] Eyring, and Polanyi[2] more than 60 years ago, the hydrogen-atom, hydrogen-molecule exchange reaction has been regarded as the benchmark system in the field of chemical reaction dynamics. The presence of only three nuclei and three electrons makes it amenable to the most exact calculations for a reactive $A+BC$ system. In the past decade, considerable progress for this reaction system has been made in both theory and experiment. Attention is called to the extensive literature devoted to quasiclassical[3–20] and quantum scattering computations[12,21–32] of integral and differential cross sections. In particular, Aoiz and co-workers[6–20] have performed quasiclassical trajectory calculations for numerous isotopic variants of the hydrogen-atom, hydrogen-molecule exchange reaction over a large range of collision energies, which has produced a relatively large database for comparison with experiment.

Experimental work in this and other laboratories was, until recently, restricted to integral cross-section measurements for reagents in the lowest and first vibrational levels, the latter achieved by the use of stimulated Raman pumping techniques. Rate constants into particular rovibrational product states have been measured in bulb experiments using resonance-enhanced multiphoton ionization (REMPI) time-of-flight (TOF) mass spectrometry[33–42] and coherent anti-Stokes Raman spectroscopy (CARS)[43–52] at relatively well-defined reaction conditions; the agreement with theory has been quite satisfactory in most cases.

Crossed-beam work on this reaction by Götting, Mayne, and Toennies,[53,54] Buntin, Giese, and Gentry,[55] and Continetti, Balko, and Lee[56] measured product differential cross sections, but owing to low signal levels and lack of resolution, it was not possible to resolve individual product quantum states. Further attempts to measure state-resolved differential cross sections in our laboratory include: reaction product imaging;[57] two-dimensional REMPI-TOF[58] of the D product; and the use of a novel molecular Rydberg-tagging scheme[59,60] to probe H+D_2→HD($v'=4,J'=3$)+D at 2.2 eV.[61] Most recently, in a series of very elegant experiments, Schnieder and co-workers[15,62] measured differential cross sections into specific rovibrational product states using a crossed-beam arrangement and D-atom-Rydberg time-of-flight detection at collision energies of 0.59 and 1.29 eV. The unprecedented resolution of these experiments has provided the best test of theoretical calculations to date in regard to the presence of dynamical resonances ca. 1.29 eV,[63] and the adequacy of different potential energy surfaces for this reaction system.[20] Further experiments by this group at collision energies of 2.2 (Ref. 64) and 2.67 eV[19] have been capable of unraveling the essential features of the scattering process, but with an energy resolution considerably worse than the one achieved at lower collision energies.

We describe a new experimental apparatus that has been constructed to carry out differential cross-section measurements for the H+D_2→HD(v',J')+D reaction using REMPI-TOF mass spectrometry and core extraction of the product laboratory velocity distribution. The paper is organized as follows: Sec. II describes the photoloc technique. Section III gives a detailed description of the experimental apparatus and explains how the photoloc technique is currently implemented. Section IV reviews the core extraction technique, and discusses how the time-of-flight instrument has been characterized using HBr photolysis and the H+HBr reaction. Section V presents the characterization of reaction conditions by measurement of the reagent rotational and translational energy distributions. Finally, in Sec. VI we

a)Electronic mail: zare@stanford.edu

show how we probe the nascent laboratory velocity distribution of specific HD(v',J') states by presenting results on the $H+D_2 \rightarrow HD(v'=2,J'=3)+D$ reaction at a collision energy of 1.55 eV.

II. THE PHOTOLOC TECHNIQUE

PHOTOLOC is an acronym for ''*photo* initiated reaction analyzed via the *l*aw *o*f *c*osines.'' This name stems from the two major elements of the technique: first, laser photolysis initiates the chemical reaction in a mixture of a photolytic precursor and reagent; second, the law of cosines relates the product laboratory velocity distribution to the center-of-mass product angular distribution. This approach has been described by Shafer-Ray *et al.*[65,66] In this section, we briefly review the underlying principles and illustrate them with examples relevant to the hydrogen exchange reaction.

The two steps in the photoloc sequence are shown in Eq. (1). Initially, a polarized laser beam photolyzes the *AX* precursor, generating *A* fragments with well-defined speed and spatial anisotropy which subsequently collide with the *BC* reagent to generate *AB* and *C* products. A second laser beam probes the $AB(v',J')$ or *C* products

$$\begin{aligned} &AX \xrightarrow{h\nu} A+X, \\ &A+BC \rightarrow AB+C. \end{aligned} \tag{1}$$

In the limit of zero relative speed between *AX* and *BC*, which is achievable by coexpanding them into a vacuum, the center-of-mass speed is solely dictated by the photolysis wavelength and the nature of the photolytic precursor *AX*. The translational energy of photofragment *A* is given by

$$E_A = \left(\frac{m_A}{m_{AX}}\right)\cdot(h\nu - \Delta E_{AX}), \tag{2}$$

where the *m*'s are the masses of *A* and *AX*, $h\nu$ is the photon energy, and ΔE_{AX} is the endoergicity of the photolysis process. From Eq. (2), and the fact that *AX* and *BC* are stationary with respect to each other, the center-of-mass speed is fixed at a value

$$u_{\mathrm{CM}} = \left(\frac{m_A}{M}\right)\cdot\sqrt{\frac{2\cdot E_A}{m_A}}, \tag{3}$$

where $M=m_A+m_{BC}$, and E_A has been calculated from Eq. (2). For a specific $AB(v',J')$ product state of known endoergicity ΔE, conservation of energy and linear momentum in the center-of-mass frame yield the following expression for the magnitude of the center-of-mass speed:

$$u_{AB} = \left(\frac{m_C}{M}\right)\cdot\sqrt{\frac{2\cdot\left(\left(\frac{\mu}{m_A}\right)\cdot E_A - \Delta E\right)}{\mu'}}, \tag{4}$$

where μ and μ' are the reduced masses of the reagent and product collision partners, respectively. Finally, the product laboratory velocity v_{AB} is the vector sum of u and u_{AB} as given by Eqs. (2) and (3), namely

$$v_{AB}^2 = u_{\mathrm{CM}}^2 + u_{AB}^2 + 2\cdot u_{\mathrm{CM}}\cdot u_{AB}\cdot\cos\theta_r, \tag{5}$$

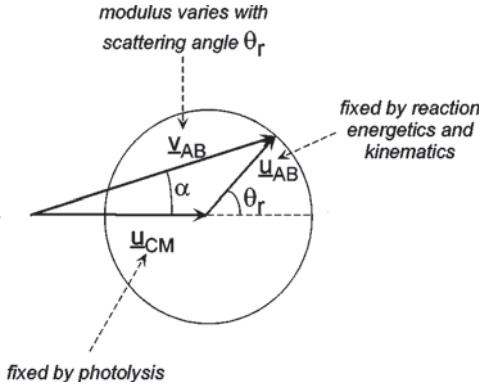

FIG. 1. Collapsed Newton diagram pertinent to the photoloc technique. For detection of a particular $AB(v',J')$ state the only vector in this figure with a variable modulus is $\underline{v}_{AB}$, the laboratory product speed. This change in modulus can be mapped directly into a change in center-of-mass scattering angle θ_r.

where θ_r is the center-of-mass scattering angle. An excellent way to picture the above quantities given by Eqs. (1)–(5) is to use a ''collapsed'' Newton diagram as shown in Fig. 1. The straightforward trigonometric relationship between v_{AB}, u, and u_{AB} is very clear and it immediately implies that a measurement of the product laboratory speed distribution can be related to the center-of-mass angular distribution, i.e., the product differential cross section.

For the case of a single photolysis channel with anisotropy β_{phot}, one-photon photodissociation with linearly polarized radiation yields a spatial distribution of photofragment *A* laboratory speeds of the form[67]

$$f(\underline{u}_A) = \frac{(1+\beta_{\mathrm{phot}}\cdot P_2(\hat{\underline{u}}_A\cdot\hat{\underline{\varepsilon}}))}{4\pi}, \tag{6}$$

where $\hat{\underline{u}}_A$ and $\hat{\underline{\varepsilon}}$ are unit vectors corresponding to the photofragment velocity and photolysis laser polarization, respectively, and P_2 is the second Legendre polynomial. The argument in the second Legendre polynomial is simply the cosine of the angle between the velocity vector of the photofragment and the direction of the laser polarization. This expression leads to the familiar perpendicular and parallel angular distributions typically found in photodissociation experiments.

From the above considerations, it is not surprising to find that if Eq. (6) governs the photodissociation step, then the laboratory distribution of *AB* product velocities is given by an analogous expression[65]

$$\begin{aligned} f(\underline{v}_{AB}) = &\left(\frac{1}{2\cdot v_{AB}\cdot u_{\mathrm{CM}}\cdot u_{AB}}\right)\cdot\left(\frac{1}{\sigma}\cdot\frac{\partial\sigma}{\partial\Omega}\right)\cdot[1+\beta_{rxn}(\underline{v}_{AB}) \\ &\cdot P_2(\hat{\underline{v}}_{AB}\cdot\hat{\underline{\varepsilon}})]. \end{aligned} \tag{7}$$

This expression has been defined so that it is normalized to unity. The similarities between Eqs. (6) and (7) are striking in the sense that for a single laboratory product speed, the spatial distribution has the same functional form as that of a photodissociation experiment with an anisotropy given by $\beta_{rxn}(\underline{v}_{AB})$. It follows that the total distribution of laboratory product speeds is a weighted sum of photolysis-like spa-

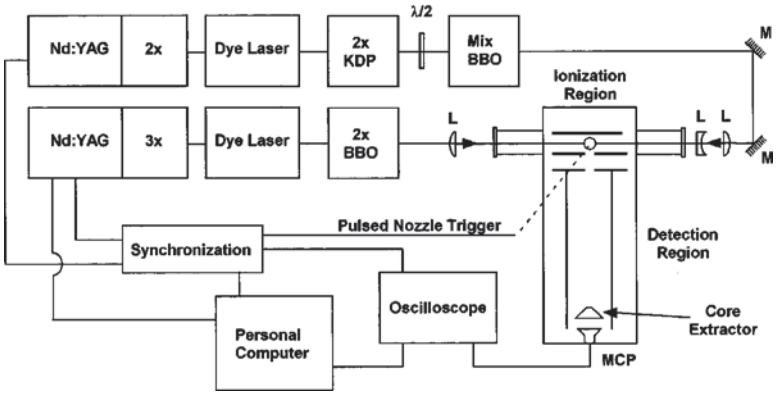

FIG. 2. Schematic block diagram of the current experimental setup. The photolysis and probe laser beams traverse the ionization chamber perpendicular to both the time-of-flight and nozzle axes (not shown). For clarity, only one probe laser setup has been shown (see the text for details).

tial distributions, the weights being proportional to the differential cross section for reaction at a particular scattering angle. Referring to Fig. 1, we find that the product anisotropy is related to the photolysis anisotropy by

$$\beta_{rxn}(\underline{v}_{AB}) = \beta_{\text{phot}} \cdot P_2(\hat{\underline{v}}_{AB} \cdot \hat{\underline{u}}_{\text{CM}}) \quad \text{and}$$

$$\hat{\underline{v}}_{AB} \cdot \hat{\underline{u}}_{\text{CM}} = \cos\alpha = \frac{v_{AB}^2 + u_{\text{CM}}^2 - u_{AB}^2}{2 \cdot v_{AB} \cdot u_{\text{CM}}}, \tag{8}$$

where α is the angle between the center-of-mass velocity and the laboratory product velocity. From Fig. 1, we can see that $\underline{v}_{AB}$ has a maximum and minimum value corresponding to the vector addition of the center-of-mass vectors in a parallel and antiparallel fashion, i.e., forward and backward center-of-mass scattering. It is precisely this range of laboratory speeds which determines the feasibility of a photoloc experiment. Following the formalism of Shafer *et al.*, we define γ as the ratio of the product center-of-mass speed and the speed of the center of mass,

$$\gamma = \frac{u_{AB}}{u_{\text{CM}}} = \left(\frac{m_C}{m_A}\right) \cdot \sqrt{\left(\frac{(\mu \cdot E_A) - (m_A \cdot \Delta E)}{\mu' E_A}\right)}. \tag{9}$$

For the $H+D_2 \rightarrow HD(v',J')+D$ reaction with $\Delta E = 0$, Eq. (9) gives $\gamma \approx 1.6$, a value quite close to the optimal case of unity. The exact value of this parameter depends on the specific $HD(v',J')$ state probed. In all cases of interest, it is close enough to the stated value, and the range of laboratory speeds is large enough to obtain angular information from the velocity distribution.

The other limit of interest is $u_{AB} \gg u_{\text{CM}}$, i.e., large γ, which is exhibited by reactions of the type $L+LH \rightarrow LL+H$, where L stands for light and H for heavy. In this case, the LL product assumes nearly a single value of the laboratory speed. From a measurement of the product angular anisotropy $\beta_{rxn}(v_{AB})$, however, we can still obtain some angular information, i.e., a root-mean-squared scattering angle. This situation is the case for the $H+HBr \rightarrow H_2(v',J')+Br$ reaction where $\gamma \approx 60$. In this case, there is essentially only one laboratory speed; this fact will be used to our advantage in later sections to characterize the experimental apparatus.

So far, we have made no mention how this distribution can be measured in the laboratory. To date, several methods have been proposed to achieve this goal. All of them attempt to measure the velocity distribution along a given laboratory axis and from this measurement infer the three-dimensional velocity distribution. For example, measurement of the Doppler profile along the laser axis has been utilized by several groups in the context of inelastic scattering[68–71] and chemical reaction dynamics.[72–75] In our laboratory, we have used two-dimensional REMPI-TOF[58] to measure the velocity distribution of the D product from the $H+D_2$ reaction along the time-of-flight axes using impulse-extraction time-of-flight mass spectrometry. A similar approach was later used to measure the $HD(v'=4,J'=3)$ product from the same reaction.[61] Alternatively, Simpson *et al.*[76] have pioneered the core-extraction technique for the study of the reactions of $Cl+CH_4$,[77–79] and $Cl+C_2H_6$.[80–83] The work presented here follows the second approach to the measurement of laboratory velocity distributions.

III. EXPERIMENTAL APPARATUS

Figure 2 shows a schematic diagram of the experimental apparatus currently employed in the study of the hydrogen exchange reaction. The setup can be subdivided into four parts: vacuum chamber and reagents, time-of-flight spectrometer, optical setup, and data acquisition.

A. Vacuum chamber and reagents

The vacuum chamber (Fig. 2) consists of two differentially pumped chambers, connected by a 6-mm diameter hole and separately pumped by two 6-inch, liquid-nitrogen-baffled diffusion pumps (Varian VHS-6 in the ionization region, and Varian M-6 in the detection region). Typical base pressures in both chambers are 5.0×10^{-8} Torr as measured by a Bayard–Alpert ionization gauge. Under normal operating conditions, i.e., nozzle firing at 10 Hz with 300 Torr stagnation pressure, chamber pressures rise to $1.0–3.0 \times 10^{-5}$ Torr in the ionization region and to $5.0–10.0 \times 10^{-7}$ Torr in the detection region.

The ionization region is equipped with two baffled, antireflection (AR)-coated, fused silica windows for the entrance of the photolysis and probe laser beams. We use a counterpropagating geometry perpendicular to the time-of-flight axis. The ionization region also houses the extraction and acceleration stages of the time-of-flight spectrometer, described in more detail in the next section. Photolysis and reaction take place in the extraction region. The pulsed

nozzle valve (General Valve Corporation, series 900 pulsed solenoid valve, 0.50 mm orifice) is driven by an IOTA ONE (General Valve Corporation) pulse driver, and it is typically used to deliver gas pulses of duration between 400 and 600 μs. The nozzle is attached to an *xyz* vacuum manipulator (Vacuum Generators), and can be translated as close as 8 mm (16 nozzle diameters) to the center of the extraction region, where reaction takes place. The nozzle axis is perpendicular to both the laser beams and the time-of-flight axis. A nude ionization gauge (Granville–Phillips 274-025), conveniently located to one side of the nozzle axis, is used to generate H_2, HD, and D_2 molecules in high vibrational levels by flowing a small amount of gas over the filament at chamber pressures on the order of 10^{-5} Torr. This vibrationally excited molecular sample is used to find the spectroscopic transitions of the reaction products of interest.

The detection region contains the free-drift tube of the time-of-flight spectrometer. It also houses the microchannel plate (MCP) detector assembly. The detector consists of two, one-inch, impedance-matched MCPs (Galileo Corporation) arranged in a chevron configuration for optimal gain. The total voltage drop across the plates is typically 2.0–2.4 kV. A 90% transmission ion grid isolates the detector from the free-drift region to avoid electric field leakage.

HBr (Matheson, 99.8% purity) and D_2 (Cambridge Isotope Laboratories, 99.8% purity) are used as reagents. The HBr reagent is further purified by repeated freeze–pump–thaw cycles with liquid nitrogen immediately prior to use. The reactive mixture is a 1:4 mixture of HBr and D_2. The vacuum manifold consists of a Teflon-lined stainless-steel reservoir and a cold finger for reagent purification. The manifold is periodically passivated by heating it to 150 °C. Gases are fed into the chamber via a Teflon line kept in a cold bath at temperatures ranging from −20° to 0 °C to avoid accumulation of contaminants in the pulsed solenoid valve during experimental runs. The operating stagnation pressure (usually 300 Torr) is regulated by the use of a micrometer valve, and monitored with a diaphragm-type Baratron gauge.

B. Time-of-flight spectrometer

Figures 3 and 4 present detailed diagrams of the time-of-flight spectrometer. The instrument consists of an extraction, acceleration, and free-drift region. For this particular type of three-stage time-of-flight spectrometer, Wiley and McLaren[84] have shown that it is possible to attain space-focusing conditions, i.e., the ion arrival time is largely insensitive to the position of the ion at time zero. For the geometry of our instrument, Wiley–McLaren conditions are attained if the voltages of the repeller, extractor, and TOF plates are set at $+V$, $-V$, and $-cV$, respectively, where c is a constant close to 7.2. The absolute magnitude of V determines the ion arrival time. This choice of voltages also ensures that the center of the extraction region, where the reaction takes place, is at a potential of zero volts. By translating the probe laser beam across the extraction region, we ensure that the Wiley–McLaren conditions are met by checking that the operating voltages yield position-independent time-of-flight profiles.

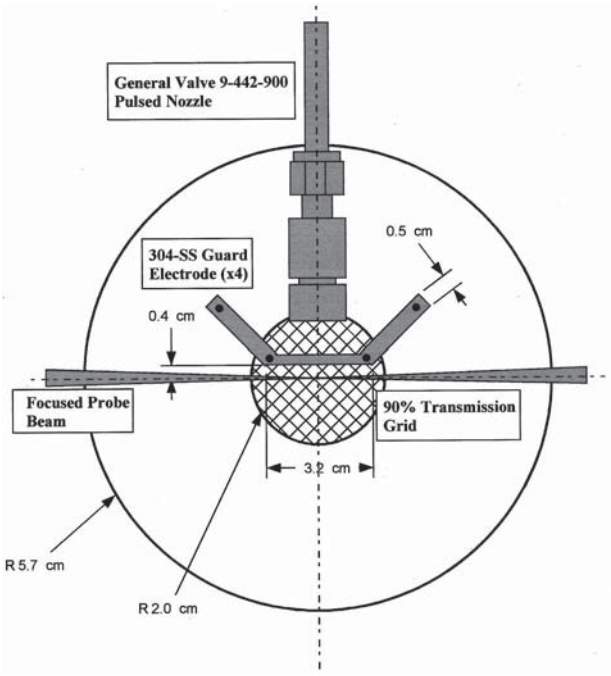

FIG. 3. Detail of the extraction region showing the nozzle valve, guard electrodes, and extraction plate assembly.

Figure 3 shows an enlarged view of the extraction region, which is equipped with a set of four stainless-steel guard electrodes equally separated by 0.46 cm. The guard electrodes run parallel to the extraction and repeller plates, and are held at well-defined voltages intermediate between $+V$ and $-V$. The latter is achieved by using a resistive voltage divider to step down the voltage from $+V$ (repeller plate) to $-V$ (extractor plate). Each electrode receives a voltage according to its position so as to provide a constant electric field strength in the extraction region. The primary function of these electrodes is to prevent penetration of stray fields into the probe region. These stray fields arise from the proximity of the stainless-steel pulsed nozzle, which is kept at a potential of zero volts. Even though we also keep the center of the extraction region at a potential of zero volts, the physical size of the nozzle can cause, in the absence of the guard electrodes, distortions of the electric field lines in areas of the extraction region sampled by ions as they are pushed toward the detector. The effect of these distortions on the time-of-flight line shapes can seriously complicate the analy-

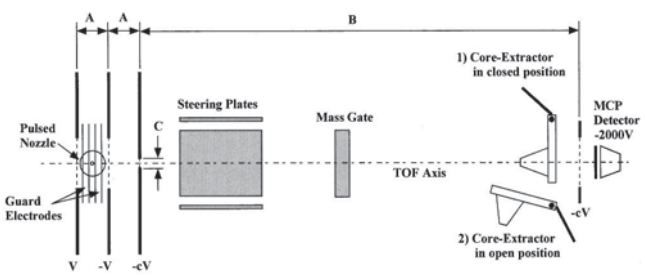

FIG. 4. Bottom view of the time-of-flight apparatus showing the extraction (Fig. 3), acceleration, and free-drift regions of the instrument ($A=2.3$ cm, $B=34.3$ cm, and $C=0.6$ cm).

sis of the experimental ion signals. Therefore, it is necessary to minimize these artifacts to the point we are no longer sensitive to changes in the time-of-flight profiles as the pulsed nozzle is translated inside the extraction region. The proper function of the guard electrodes has been tested via computer simulation of the instrument using the ion-optics software SIMION.[85] Simulations of ion trajectories with this program were particularly useful in the early stages of the design of the time-of-flight spectrometer. These simulations provided us with a reasonable set of distances and dimensions for the guard electrodes which showed no significant electric field leakage from the pulsed valve into the probe region. Later, we also checked experimentally the effect of nozzle proximity on flight times and peak shapes, and found no distortions of the experimental time-of-flight profiles under normal operating conditions.

The free-drift region (Fig. 4) has a set of horizontal and vertical steering plates. Their voltage can be continuously varied about $\pm 10\%$ of the total TOF voltage to aid proper steering of the ion packet onto the detector. A mass gate is used to avoid detection of high-mass backgrounds. This suppression is achieved by applying a 10 ns rise time, 100–300 V pulse to the mass gate plate for a few microseconds and has proven to be quite efficient at increasing the lifetime of the MCPs.

A set of two core extractors of variable diameter (currently 3 and 1 mm radii) can be placed along the TOF axis with the aid of vacuum manipulators (Vacuum Generators). Time-of-flight profiles can be obtained with or without the core extractor in place, depending on the purpose of the experiment, i.e., integral or differential cross-section measurements.

C. Optical setup

Linearly polarized photolysis radiation in the range of 200–300 nm and output powers ranging from 5–20 mJ pulse are obtained by frequency doubling (KDP) and mixing (BBO) the output of a dye laser (Spectra-Physics PDL-2) pumped by the second harmonic of an Nd:YAG laser (Spectra-Physics GCR-5). This setup allows the generation of H atoms at collision energies between 0.5–2.5 eV by the use of either HBr or HI as photolytic precursors. The results described in this paper will be restricted to the use of HBr. The doubled or tripled output of this laser is separated from the fundamental beams by the use of dichroic mirrors. The beam, originally 7–8 mm diameter, is collimated by a 3:1 Galilean telescope whose output is steered into the vacuum chamber. Collimation ensures that a large fraction of the precursor is photolyzed and also minimizes undesirable light scattering in the time-of-flight region.

Probe laser frequencies ranging from 200–500 nm are generated by various means. The $E,F\,^1\Sigma_g^+ \leftarrow X\,^1\Sigma_g^+(2+1)$ REMPI scheme is a well-established technique[86–90] for the detection of H_2 and its isotopomers. The transitions for the first five ground-state vibrational levels lie in the 200–250 nm region. Probe powers between 1.0 and 3.0 mJ/pulse in this wavelength region are achieved by: (1) frequency tripling the red output of a dye laser (Lambda Physik SCANMATE 2E) pumped by the second harmonic of a seeded Nd:YAG laser (Spectra-Physics GCR-4), (2) frequency doubling and 1064 nm mixing the yellow or green output of a dye laser (Lambda Physik LPD 3000) pumped by a seeded Nd:YAG laser (Spectra-Physics GCR-3), and (3) frequency doubling the blue output of a dye laser (Lambda Physik LPD 3000) pumped by the third harmonic of a seeded Nd:YAG laser (Spectra-Physics GCR-4). The UV output is separated and expanded with a 1:3 Galilean telescope prior to being focused by a 50–80 cm fused silica positive lens. We have found that the use of a telescope prior to focusing the beam enhances the two-photon process by at least one order of magnitude. The linewidth of each probe laser is around 0.25 cm^{-1} in the fundamental as measured with an etalon.

Half-wave plates (Optics for Research and CVI Corporation) specifically designed to operate at these wavelengths control the polarization of both the photolysis and probe lasers.

D. Data acquisition

A 10-Hz, homemade master clock is used to trigger the experiment. A set of four digital delay generators (Stanford Research Systems DG535) control the timing of the photolysis and probe lasers as well as the nozzle pulse driver, oscilloscope, and TOF mass gating. Ions arriving at the detector are sent via shielded RG-59 cable to a 500 MHz digital oscilloscope (Tektronix TDS620). The TOF profiles are digitized and sent to a PC (Pentium 133 MHz) via an interface box (Stanford Research Systems SRS245) and GPIB interfaces (National Instruments).

We use the oscilloscope in two different data acquisition modes. In the first mode, we simply acquire the digital oscilloscope traces and average over a given number of shots to obtain a TOF profile. This acquisition mode is suited to measure time-of-flight profiles arising from a high-yield process such as a one-photon photodissociation. In the second mode, we use the oscilloscope as an ion-counting device by specifying start and stop triggers and a dead time between single ion counts. This data collection scheme is well suited to detect the low signals arising from chemical reactions. In addition, the use of single-ion counting allows us to avoid signal distortion and ringing associated with impedance mismatches at the detector.

IV. INSTRUMENT CHARACTERIZATION

A. Core-extracted signal analysis

The goal of core extraction is to obtain the velocity distribution along the time-of-flight axis by rejecting ions with any off-axis speed components. In practice, this task is achieved by placing a conical mask of a given radius at the end of the time-of-flight tube before the MCP detector (Fig. 4). In the limit of ideal core extraction, a single-speed component along the measurement axis is given by two delta functions, corresponding to those ions traveling toward and away from the detector. Our Wiley–McLaren TOF spectrometer ensures that these two peaks are equally spaced in the time-of-flight profile with respect to the arrival time of a static sample. In practice, ideal core extraction cannot be

realized because of the finite size of the core extractor necessary to attain reasonable signal levels. Thus, we need a compromise between these two factors and therefore we must characterize the instrument function with known velocity distributions over a wide range of operating conditions. A calibration gives us the ability to generate a faithful representation of the single-speed basis functions necessary to convert the laboratory speed distribution into a center-of-mass angular distribution.

A Monte Carlo simulation of an ion packet propagated through the instrument generates the single-speed basis functions. The input to the simulation includes the speed of the ion packet, its spatial anisotropy, the orientation of the laser polarization with respect to the time-of-flight axis, the instrument voltage settings, the linewidth of the probe laser (assumed to be at the center of the resonance), and two parametrized blurring functions that account for the resolution of the instrument.

Several factors affect resolution in a core-extracted time-of-flight profile. The first and most obvious one is the finite duration of the probe laser pulse, which in our case blurs the time zero in the time-of-flight profile by at least 4–5 ns. In addition, the core extractor has a finite size causing some ions with a nonmaximal speed component along the time-of-flight axis to be detected. Other blurring effects may include imperfections in the instrument and lack of control over the initial conditions such as the thermal spread of the reagents that lead to reaction product. We have chosen, in the same spirit as Simpson *et al.*,[76] to parametrize the instrument blurring by using two arbitrary functional forms that attempt to account for all the factors affecting resolution along the longitudinal and transverse directions with respect to the TOF axis. Longitudinal blurring has been modeled with a Gaussian functional form. Transverse blurring is accounted for by calculating the transmission of an ion through a core extractor subjected to an exponentially decaying transmission probability at each point across the core extractor area. The validity of these parametrizations is only guaranteed if they are capable of modeling satisfactorily single-speed distributions. Sections IV B and C describe the results obtained for single-speed distributions arising from the photolysis of HBr and the H+HBr reaction. A further discussion of these instrumental parameters will be deferred until then.

With knowledge of the instrument function, we can construct a basis set spanning the velocity range pertinent to the problem. In general, a time-of-flight profile $S(t)$ is taken to be a linear combination of speed basis functions $B_i(t)$,

$$S(t)=\sum_{i=1}^{N} c_i B_i(t), \tag{10}$$

where the maximum number N of basis functions is given by the speed resolution of the instrument, which varies depending on the extraction conditions. At this point, the problem is reduced to finding the coefficients c_i of this expansion via a least-squares fitting procedure. We have used two different fitting approaches: singular-value decomposition[91] and simulated annealing combined with a maximum entropy algorithm.[73,76] Both approaches yield very similar results, provided that the signals are not subjected to excessive noise and the covariance between basis functions is sufficiently small, i.e., the core-extracted basis functions are reasonably close to the limit of being an orthonormal set.

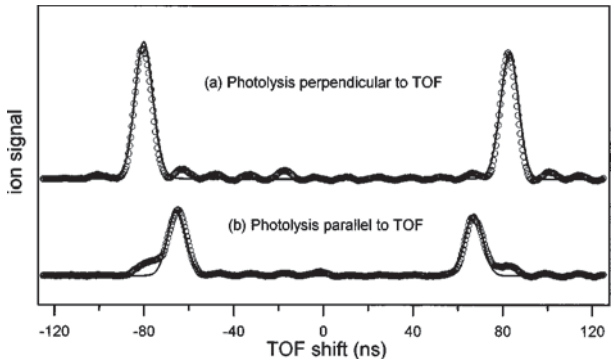

FIG. 5. Core-extracted, H-atom time-of-flight profiles from the photodissociation of HBr at 243 nm at two photolysis polarization geometries. The upper trace corresponds to the fast channel, correlating with ground-state Br atoms and with an anisotropy of $\beta=-1$. The lower trace corresponds to the slow photolysis channel with $\beta=+2$. The solid lines are fits to the experimental profiles using the instrumental parameters given by the first row of Table I (50 V extraction voltage).

To obtain the differential cross section, we need to convert the coefficients in Eq. (10), which describe the contributions of each laboratory speed to the signal, into the corresponding angular coefficients. The Jacobian of the transformation between the speed distribution $P(v_{AB})$ and the angular distribution $P(\cos\theta_r)$ is given by

$$P(\cos\theta_r)=\left(\frac{u\cdot u_{AB}}{v_{AB}}\right)\cdot P(v_{AB})=2\pi\frac{1}{\sigma}\left(\frac{\partial\sigma}{\partial\Omega_r}\right), \tag{11}$$

where θ_r and v_{AB} are related to each other through the law of cosines as shown in Eq. (5). The last term is the normalized differential cross section into solid angle Ω_r.

B. HBr photolysis

One-photon photolysis of hydrogen bromide molecules by UV radiation generates fast and slow H atoms correlating with Br($^2P_{3/2}$) and Br($^2P_{1/2}$), respectively.[92] The slow H-atom branching fraction and anisotropy parameters for each product channel are wavelength dependent and have been measured for the HBr molecule at 193 nm by Xu, Koplitz, and Wittig,[93] at 243 nm by Kinugawa and Arikawa,[94] and more recently by Regan *et al.*[95] over the 201–253 nm wavelength range.

We have carried out experiments to measure the core-extracted HBr velocity distributions at 243 and 217 nm, the latter being the photolysis wavelength of the reactive scattering experiments described in the following sections. Detection of the hydrogen atom was achieved by the use of the familiar (2+1) REMPI scheme of hydrogen via the $1s\,^2S_{1/2}\rightarrow 2s\,^2S_{1/2}$ transition. Figure 5 shows a representative core-extracted profile from photolysis at 243 nm, using the same laser to photolyze the HBr reagent and to probe the H-atom photofragment. Figures 5(a) and 5(b) are TOF profiles for two different photolysis polarizations. These figures also present the fits to the experimental profiles using the procedures described in Sec. IV A. Similar data have been taken at

TABLE I. Time-of-flight instrumental function parameters[a] obtained from the HBr photodissociation experiments.

Extraction voltage (V)	Longitudinal resolution (ns)	Transverse resolution (mm)	Velocity resolution for m/e=1 (m/s)
50	9	3	1700
100	7	2	2100
200	5.5	1	4200

[a]Parameters shown in this table are for a 3-mm radius core extractor.

TABLE II. HBr photodissociation results.

Photolysis wavelength (nm)	v_{fast} (km/s)	v_{slow} (km/s)	β_{fast}	β_{slow}	Slow channel branching fraction Br*/(Br+Br*)
243	16.0	13.0	−1	+2	0.16±0.02[a]
217[b]	19.3	16.9	−1	+1.4–1.6	0.14±0.03

[a]Error bars in the slow channel branching fraction represent one standard deviation from the mean of a total of five measurements at each photolysis wavelength.
[b]Photolysis anisotropies at 217 nm have been obtained from the best fit using the calibration parameters obtained at 243 nm.

217 nm using a two-laser setup to carry out the photolysis and subsequent detection of the hydrogen photofragment. From Fig. 5, the presence of a perpendicular and a parallel H-atom channel is quite clear, the faster corresponding to a $\beta_{phot}=-1$ and the slower one to $\beta_{phot}=+2$.

Table I summarizes the results of the fits for signals collected at various extraction voltages. Varying the extraction voltage is equivalent to changing the size of the ion packet being imaged onto the detector. The trends found in the longitudinal and transverse blurrings are similar to those found for the Cl_2 photodissociation calibrations carried out in this laboratory on a similar instrument.[96] There is a slight absolute increase in the longitudinal and transverse widths as the extraction voltage is diminished, i.e., as the ion packet has more time to expand in the time-of-flight region. Nonetheless, a decrease in the extraction voltage enhances the speed resolution of the instrument. The speed resolution quoted in the last column of Table I corresponds to a mass-to-charge ratio of unity. This resolution needs to be divided by the mass of the ion being detected in order to determine the speed resolution of ions of a different mass under the same TOF conditions. The temporal spread of the H-atom ion signals corresponds roughly to the temporal spread expected for the HD(v',J') product from the hydrogen exchange reaction. This relation holds because the change of the arrival time corresponding to a given initial speed along the detection axis scales linearly with mass, and the speed of the H-atom reagent is at least three times larger than that of the HD(v',J') product. Moreover, the values shown in Table I can equally apply to any mass of interest to this work, provided we first determine for a given laboratory speed and mass the spatial size of the ion packet at the time of core extraction.

From the measurements shown in Fig. 5 and given in Table I, we determined a slow channel branching fraction of 0.16±0.02 at 243 nm. This value is in agreement, within experimental uncertainties, with the value of 0.17±0.02 most recently reported by Regan *et al.*[95] Table II summarizes the results of the photodissociation studies carried out at 217 and 243 nm. Within our experimental uncertainty, the branching fraction is the same at both wavelengths, in agreement with the results of Regan *et al.*,[95] who have performed a more systematic study of HBr photolysis over a wide range of photodissociation energies.

Examination of the slow channel time-of-flight profile at 217 nm also suggests a deviation of the anisotropy parameter from the maximal value of +2 found at 243 nm. If we take the calibration parameters obtained from the results of the photodissociation of HBr at 243 nm, we find that the best fit for the data at 217 nm is obtained with a $\beta_{slow}=1.4-1.6$, also in agreement with the work of Xu, Koplitz, and Wittig[93] and Regan *et al.*,[95] whose results show a clear dependence of the anisotropy of the slow product channel over the 193–250 nm range.

It should be noted that the HBr branching fraction is at least a factor of 2 smaller than that found for the HI molecule at similar frequencies, thus making HBr a cleaner source of fast H atoms. This behavior is advantageous in those cases in which a given HD rovibrational product state can be populated by both photolysis channels. The combination of a small slow H-atom yield, a smaller rate constant for reaction, and an experimental geometry favoring product detection arising solely from the fast channel reduces or essentially eliminates the contribution from the slow H-atom channel to the detected HD signal.

In addition, we have found that HBr is a more suitable precursor than HI from a purely practical point of view. Experiments with HI at the same wavelengths precluded the measurement of reliable speed distributions owing to intense I^+ and HI^+ backgrounds. These backgrounds cause severe space-charge effects that distort the velocity distributions of the nascent HD(v',J') product. We attribute the appearance of these backgrounds to the direct, two-photon ionization of I and HI by our focused probe laser. Direct two-photon ionization of HI is energetically possible below 240 nm, whereas for HBr this threshold is shifted to 210 nm. As a consequence, we have greatly reduced high-mass backgrounds by the use of the HBr photolytic precursor.

C. $H_2(v'=4,J'=1)$ product from the H+HBr reaction

Both the H+HI and H+HBr reactions are known to produce H_2 with a large amount of vibrational and rotational excitation. This property has been exploited by Heck *et al.*[90] to perform the spectroscopy of the $E,F\,^1\Sigma_g^+-X\,^1\Sigma_g^+$ system of D_2 for large rotational and vibrational quantum numbers arising from the D+DI reaction. Similarly, Kliner *et al.*[97] have studied the H+HI reaction in this laboratory prior to the measurement of integral cross sections for the hydrogen exchange reaction. In our particular case, the H+HBr reaction has been useful mainly because the kinematics of this reaction allow it to be used as a prototype of a chemical reaction resulting in a single-speed distribution.

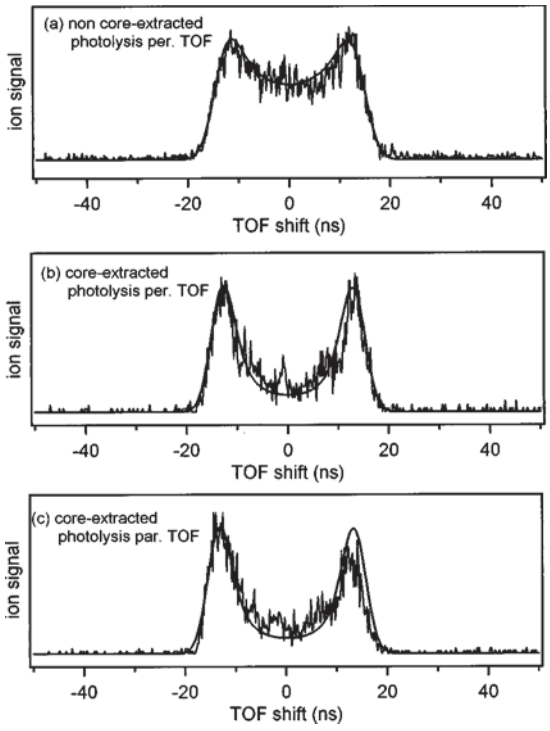

FIG. 6. (a)–(c) Time-of-flight profiles of the $H_2(v'=4,J'=1)$ product from the H+HBr reaction at a collision energy of 1.9 eV. The H_2 product displays a single laboratory speed ca. 9000 m/s. Solid lines are fits to the experimental profiles.

Chemical reactions studied by the photoloc technique have, in general, uncertainties in the reactive step from thermal motion of the reagents. For this reason, we decided to examine the H_2 product from this reaction to make sure that the calibration parameters obtained from the HBr photodissociation studies could be used reliably for the continuous distribution of laboratory speeds that characterize the HD product from the $H+D_2$ reaction.

Figure 6 shows the velocity distribution of the $H_2(v'=4,J'=1)$ product at a collision energy of 1.9 eV (photolysis wavelength of 217 nm). For this particular H_2 product state, there is a possibility of both photolysis channels leading to this rovibrational level. As the core-extracted TOF profiles in Figs. 6(b) and 6(c) show, however, we only find evidence for one speed, that belonging to the fast photodissociation channel. All three TOF profiles are satisfactorily fit by a product speed of 9000 m/s, and the instrumental function parameters are very similar to those of the HBr photolysis studied at the same voltage conditions. In general, we have found that the reactive product tends to require a slightly larger transverse blurring parameter caused by factors not present in simple photolysis experiments.

From Figs. 6(b) and 6(c), taken at two different photolysis-probe geometries, the anisotropy of the velocity distribution is essentially zero, i.e., the profile intensity is independent of laser polarization. This measurement implies a vanishing second-order moment of the angular distribution, that is, $\langle P_2(\cos\theta_r)\rangle=0$. While the kinematics prevent us from obtaining complete angular information, this result implies that the H_2 product is not exclusively back-scattered or forward-scattered. If this were the case, the anisotropy of the time-of-flight would approach the photolysis anisotropy, in this case -1. This result is consistent with the experimental work and semiclassical calculations on the H+HX family of reactions by Valentini and co-workers.[98–100]

In addition, the noncore-extracted profile shown in Fig. 6(a) contains additional information regarding the Doppler selectivity of the probe laser. For a $\beta=0$ distribution, this profile should not display a minimum in the center, but should be flat. The dip in the profile arises from the Doppler selection of the probe laser which discriminates against those ions with large speed projections along the laser axis. A Lorentzian line shape with a FWHM of 2000 m/s was necessary to properly fit the noncore-extracted signal satisfactorily. This Doppler selectivity agrees closely with previous measurements of the laser linewidth which include: (1) measurement of the fundamental laser linewidth with an etalon, (2) deconvolution of peak line shapes arising from H_2, D_2, and HD(2+1) REMPI resonances, and (3) peak line shape analysis of the Kr(2+1) REMPI resonance at 222.6 nm,[101] where the effect of Doppler broadening can be neglected owing to the large mass of this atom.

V. CHARACTERIZATION OF REACTION CONDITIONS

Paramount to the use of the photoloc technique is the experimental realization of the assumptions presented in Sec. II. It is necessary, for example, to have a knowledge of the initial internal energy distributions of the reagents in order to evaluate all possible sources resulting in a degradation of resolution. Furthermore, a close comparison with theory requires that we know the collision energy resolution of the experiment as well as the number of rotational levels populated in the diatomic reagent. For this purpose, we have carried out an extensive characterization of the HBr and D_2 rotational and translational distributions under the experimental conditions used in the HBr, H+HBr, and $H+D_2$ experiments.

In an attempt to optimize the reaction conditions, we have measured these distributions at several nozzle delays, stagnation pressures, and distances of the nozzle from the photolysis-probe region in the TOF apparatus. The results described below correspond to the best overall conditions that are compatible with reasonable product signal levels. In general, we have found that the optimum time to probe for reactive product is located near the front of the nozzle pulse. This is about 150–200 μs after the first appearance of ion signal from either reagent for a typical gas pulse width of 500–600 μs. Probing the temporal center of the nozzle expansion, where the largest signal levels are expected, tends to produce distortions in the time-of-flight profiles. We attribute this behavior to ion-neutral collisions as the ions are extracted into the free-drift region.

Figure 7(a) shows the (2+1) REMPI spectrum of the first members of the Q-branch of the $H\,^1\Sigma^+ \leftarrow X\,^1\Sigma^+(0,0)$ band of HBr near 250 nm. Gordon *et al.*[102] first used this REMPI scheme in their systematic investigation of the Rydberg states of the HBr molecule. We calibrated the line-

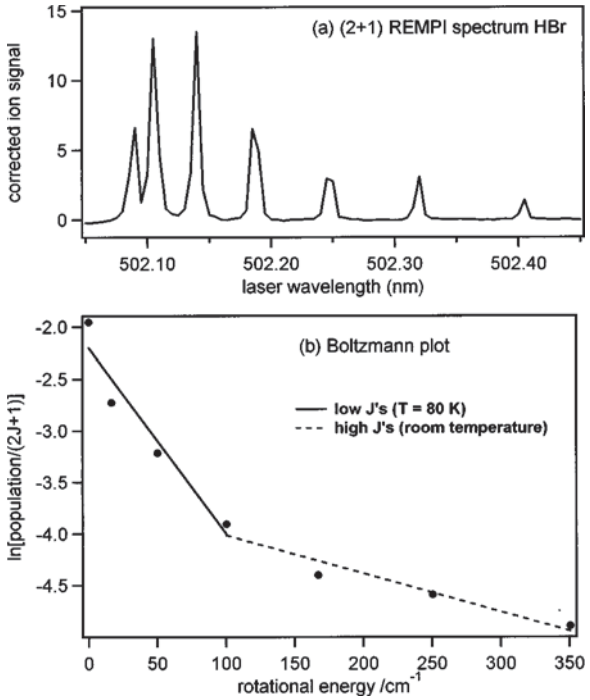

FIG. 7. (a) (2+1) REMPI spectrum of HBr, and (b) Boltzmann plot of the rotational population in the jet expansion used for the photolysis and reaction studies described in the text.

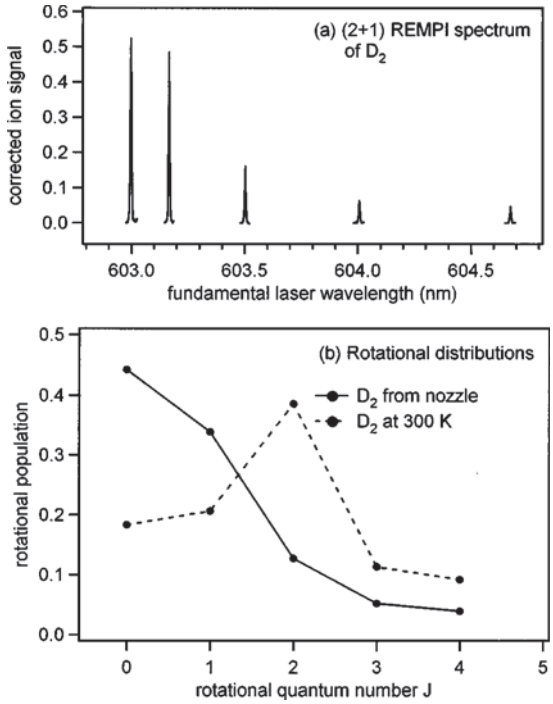

FIG. 8. (a) (2+1) REMPI spectrum of D_2 from the nozzle expansion at the same conditions as those of Fig. 7. (b) Comparison of the rotational populations in the beam and at room temperature.

strength factors by measuring the rotational distribution of a room-temperature HBr sample fed into the vacuum chamber. As expected, this branch shows essentially no dependence of the line strength on rotational quantum number. A temperature of around 80 K can be assigned for the first four states of the Boltzmann plot shown in Fig. 7(b) and a room-temperature distribution for the higher ones. This initial rotational energy distribution in the photolytic precursor results in a collision energy spread of, at most, 0.01 eV.

Figure 8(a) shows the (2+1) REMPI spectrum and the rotational distribution of $D_2(v=0,J)$ from the gas expansion at the same nozzle delay as that for HBr in Fig. 7. The rotational distribution and line-strength factors for D_2 were similarly determined from a room-temperature sample. In the case of D_2, the cooling of the rotational degree of freedom is harder to achieve than for HBr because of the larger rotational constant for D_2, and because collisions can only produce odd–odd and even–even rotational transitions. As shown in Fig. 8(b), most of the rotational population resides in levels 0, 1, and 2 with ratios approximately 0.45:0.35:0.1. A ''temperature'' of 90 K can be assigned to this distribution, if desired. This distribution should be taken into account when comparing our experimental results with theoretical predictions.

The most important source of uncertainty in our experiments comes from the initial thermal motion of the HBr and D_2 reagents, a problem that van der Zande *et al.*,[103,104] and Aoiz *et al.*,[105] have analyzed in detail in the context of photoinitiated reactions. Although we coexpand these two molecules in a vacuum, no guarantee exists that they will reach the limit of zero translational temperature. The rotational distributions presented above already provide a conservative upper limit to the translational temperature of about 80 K, which corresponds to a collision energy resolution of approximately 0.08 eV.

Fortunately, our time-of-flight instrument is capable of providing a better estimate of the translational cooling achieved during the expansion process. We have accomplished this task by comparing the TOF temporal widths of HBr and D_2 in the beam and at room temperature. Figure 9 shows the time-of-flight profile of HBr from the expansion at different regions in the nozzle pulse. The different widths in these profiles illustrate the sensitivity of this measurement to the local translational energy spread at different points in the expansion. Figure 9 also shows the width of the TOF profile expected from a thermal $H^{79}Br$ sample. The close proximity

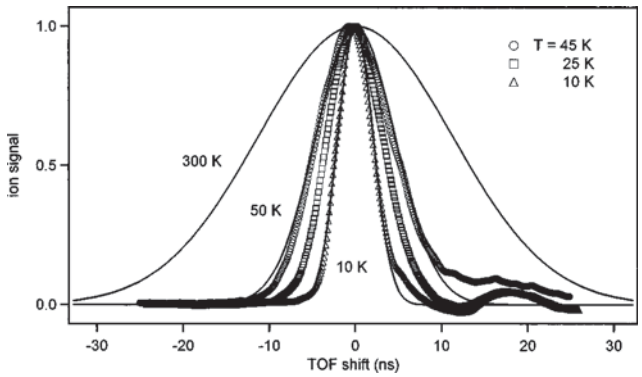

FIG. 9. HBr time-of-flight profiles at different nozzle delays are represented by symbols. Note the increase in the peak width as the nozzle delay is increased and one moves into the peak of the gas pulse (from diamonds to circles). Solid lines show the expected time-of-flight profiles at 10, 50, and 300 K taking into account the instrumental resolution.

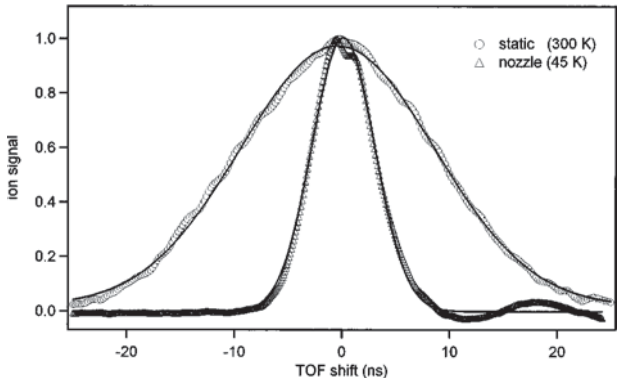

FIG. 10. Time-of-flight profiles of D_2 from the expansion, and from a room-temperature sample. The beam translational temperature is estimated to be ca. 45 K.

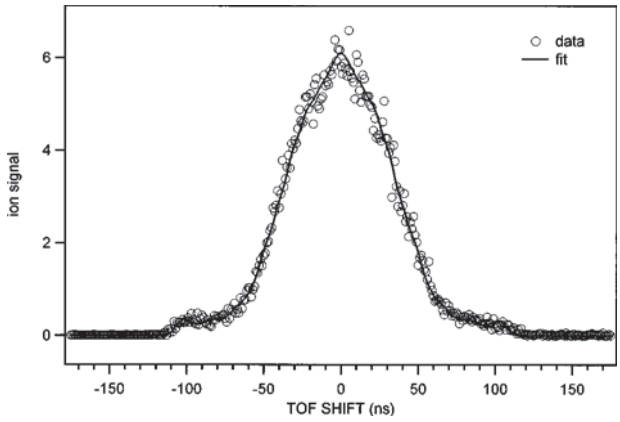

FIG. 11. Representative time-of-flight profile of the HD($v'=2,J'=3$) product from the $H+D_2 \rightarrow HD(v',J')+D$ reaction at 1.55 ± 0.05 eV from a one-laser, photolysis-probe experiment at 217 nm. The solid is the result of an SVD fit using a total of 12 basis functions spanning the whole speed range for this product state.

of ^{79}Br and ^{81}Br peaks in the TOF profile precluded direct measurement of the thermal HBr width. The solid lines in Fig. 9 correspond to fits of these signals taking into account the instrument function. The temperature inferred from these measurements varies from 10 K at the front edge of the nozzle pulse to 45 K at the region where the rotational temperatures were measured. Figure 10 shows the D_2 time-of-flight profiles at room temperature and at a nozzle delay corresponding to a HBr translational temperature of 45 K. Within our experimental uncertainty, we find that D_2 has the same temperature as the HBr precursor. From these measurements of the translational temperatures in the beam, we can conclude that reagent thermal motion does not contribute more than 0.04 eV to the spread in collision energy. This spread, combined with the previous value of 0.01 eV from the rotational energy distribution of HBr, yields an upper limit to the collision energy resolution of 0.05 eV.

A concern remains regarding a plausible ''velocity slip'' between the HBr and D_2 reagents caused by the disparity of their masses and the mild expansion conditions. The presence of this effect would, among other things, complicate the analysis of the velocity distributions and therefore should be avoided. We conclude that this effect should be negligible in our experiments, based on the translational temperatures estimated from the TOF profiles. As McClelland *et al.*[106] and DePaul, Pullman, and Friedrich[107] have discussed in their studies of seeded supersonic expansions, velocity slip becomes an issue when the species have not had sufficient time to cool their translational degrees of freedom to the same extent. In other words, slip arises from differences in the thermal distributions of the coexpanding species. Under our current experimental conditions, we estimate that the expansion has reached about 90% of the terminal expansion speed so that the estimated slip should be, at most, 50–100 m/s.

Finally, there exists the possibility that the HBr molecules become aligned during the expansion process. Recall that the photofragment velocity distribution shown in Eq. (6) assumes both a linearly polarized photon for photolysis and a randomly oriented initial distribution of bond axes.[68] The first prerequisite was fulfilled by careful control of the state of polarization of the photolysis radiation, as described in Sec. III C. The second prerequisite had to be checked experimentally, even though one could expect minimal prealignment effects because of our mild expansion conditions. Prealignment of the HBr ensemble before photolysis would necessarily require the inclusion of other Legendre moments in the derivation of the product velocity distribution for a photoinitiated chemical reaction. The HBr photodissociation data shown in Sec. IV B show that the anisotropy parameter for the fast channel is maximal ($\beta=-1$), in agreement with measurements from other laboratories using expansions at higher stagnation pressures[95] and static-gas conditions.[93] Moreover, we also performed magic-angle ($\theta=54.7°$, $P_2=0$) TOF measurements. These measurements served as a further check for the Monte Carlo simulation of the time-of-flight profiles, and showed that only up to a second Legendre moment was necessary for a description of all the experimental velocity distributions taken at different photolysis polarization angles. Therefore, we conclude that the prealignment of HBr molecules in the expansion is minimal, and the expressions of Sec. II can be used safely for the analysis of the velocity distributions arising from reaction products.

VI. DIFFERENTIAL CROSS SECTION FOR HD($v'=2,J'=3$) AT 1.55 ± 0.05 eV

The two preceding sections have described how we have carried out a detailed characterization of the instrument and the reaction conditions under which we study the $H+D_2$ reaction. We discuss here how we measure the product velocity and angular distributions for this reaction. We present results for the HD($v'=2,J'=3$) product at 1.55 ± 0.05 eV.

Figure 11 shows a representative time-of-flight profile and the fit to the signal using the calibration parameters and basis set previously described in Sec. IV. In this particular case, we used a single laser to photolyze and to detect the HD product in order to illustrate our ability to obtain velocity-sensitive data for this reaction system. The TOF profile shown in Fig. 11 is the result of ion counting a total of 20 000 laser shots, with laser powers near 0.5 mJ/pulse. The signals presented here have been measured under single-ion counting conditions, with a maximum of 150–200 ions

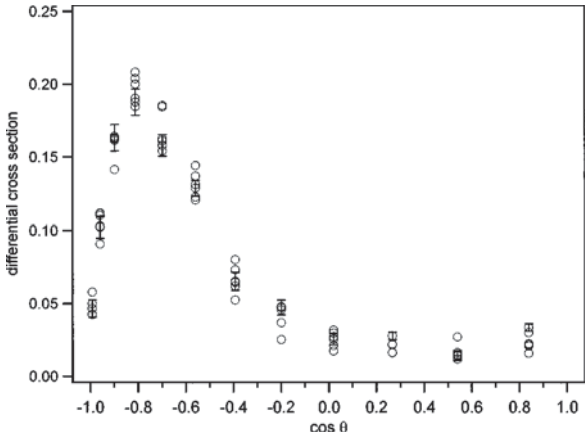

FIG. 12. Differential cross sections for the HD($v'=2,J'=3$) product obtained from six independent measurements of the velocity distribution. The error bars shown are representative of the statistical errors from each independent inversion of the laboratory velocity distribution into an angular distribution. The spread in the data points is indicative of systematic errors in our measurements.

per bin from each experimental run. The experimental conditions have been refined to the point that it is possible to obtain TOF profiles devoid of any artifacts that may arise from space-charge and collisional effects. For this purpose, the shape of the signal was carefully checked at various laser powers to avoid any of the above complications. We also checked for possible systematic errors arising from improper centering of the ion packet onto the core extractor. We accomplish this test by carefully scanning the deflection voltages and finding the center of the ion packet corresponding to reactive HD product. Similarly, we scanned carefully over the Doppler line shape of the two-photon resonance to ensure the laser was located at its center. This procedure is performed by checking both the overall shape and width of the corresponding time-of-flight profile and by ensuring that its temporal width is both symmetric and maximized.

The experimental TOF profile shown in Fig. 11 spans an approximate time width of 240 ns, matching quite accurately what would be expected given the velocity range of 100–7600 m/s corresponding to this rovibrational state. As Fig. 11 shows, the signal spans the entire laboratory speed range, but the intensity clusters around slow values, i.e., toward the backward hemisphere. From our knowledge of the instrument function, we are justified to use a total of 12 evenly spaced speed-basis functions to perform a linear least-squares fitting of the experimental profile. The inversion of the speed distribution into an angular distribution was performed by either using a direct singular-value decomposition (SVD) of the signal or by performing a simulated-annealing maximum entropy fit. In general, we have found that for reactive signals, the maximum entropy algorithm is more robust than the SVD one, especially in cases of poor signal-to-noise ratio, for which the SVD procedure tends to produce unphysical results (negative coefficients).

Figure 12 shows the angular distributions obtained from measurements of the same product state that were taken over a period of several days. The error bars for each data set were obtained from the covariance matrix of the SVD fit and are indicative of the statistical errors arising from the Poisson-like statistics of the ion-counted signals. The spread of the data between fits is directly attributable to systematic fluctuations in our measurements, such as incorrect positioning of the core extractor and slightly different reaction conditions. As evidenced from the results of these fits, the contributions from systematic errors dominate the statistical ones. Nonetheless, all six independent measurements yield the same shape for the angular distribution.

At the collision energy of these experiments, it is energetically possible for the slow channel (1.3 eV) to populate this state. As shown in Sec. IV, however, photolysis at this wavelength generates only 16% slow hydrogen atoms. In addition, photolysis-probe experiments of this type measure reaction rates into a particular level, and therefore this percentage needs to be weighted by the ratios of the relative speeds and cross sections at both collision energies. The quasiclassical (QCT) calculations of Blais and Truhlar[3,5] show that the cross section of HD($v'=2,J'=3$) at 1.3 eV is approximately a factor of 2 smaller than at 1.6 eV. Taking into account both these speed and cross-section differences, we estimate a contribution of the slow channel of 7%–8%. Moreover, the polarization of the laser has been set perpendicular to the TOF axis; this experimental geometry favors detection of reaction products arising from the fast channel (negative photolysis anisotropy), further reducing our sensitivity to the slow channel. Thus, the 7%–8% contribution quoted above can be regarded as an overestimate. The size of the systematic errors that are inferred from Fig. 11(b) is at least 10% of the total signal into any particular angular bin. We are thus confident that the shape of the differential cross section for reaction for this particular rovibrational state reflects faithfully the fast H-atom channel. We find that this cross section shows pronounced back-scattering peaking at $145°\pm10°$ with an FWHM of roughly 40°. Owing to the conversion from evenly spaced velocity basis functions to the cosine of the scattering angle, the angular resolution in these measurements varies from 5–6° in the backward region to 12–13° in the forward-scattering region.

VII. CONCLUSIONS

We have described a new experimental apparatus used to measure the product differential cross section for specific HD(v',J') levels in the $H+D_2$ exchange reaction. This paper focused on the description of the instrument and the required characterization of the time-of-flight instrument and reaction conditions. It is hoped that future work will report systematic studies of this most fundamental chemical reaction.

HBr photodissociation and the H+HBr reaction allow us to calibrate this instrument. Particular emphasis was placed on ensuring that similar sets of calibration parameters could be used to characterize single-speed distributions from both photodissociation and chemical reaction.

The reaction conditions under which we performed these experiments have been fully characterized. The collision energy resolution determined from these studies is found to be, at most, 0.05 eV, considerably lower than the value of 0.15 eV reported previously in this laboratory.[61] With this resolu-

tion, it may be possible to perform careful studies of the collision energy dependence of the differential cross section at collision energies higher than previous studies of this reaction, and with sufficient angular resolution to obtain dynamical information directly comparable with theoretical predictions.

This study presents the results of a one-laser experiment that initiates photolysis of HBr and probes the subsequent HD($v'=2$,$J'=3$) product of the $H+D_2$ reaction at 1.55 ± 0.05 eV. The current speed resolution of the instrument allows for the use of a total of 12 basis functions that span the entire angular range. Our results are in contrast to recent differential cross-section measurements of Schnieder and coworkers, who cannot detect forward-scattered product below 70–90°.[62] We defer the interpretation of our observed state-specific differential cross section until we have made a more extensive study of different rovibrational product states recorded at different collision energies.

ACKNOWLEDGMENT

The National Science Foundation is gratefully acknowledged for financial support under Grant No. CHE-93-22690.

[1] F. London, Z. Elektrochem. **35**, 552 (1929).
[2] H. Eyring and M. Polanyi, Z. Phys. Chem. Abt. B **12**, 279 (1931).
[3] N. C. Blais and D. G. Truhlar, Chem. Phys. Lett. **102(2,3)**, 120 (1983).
[4] N. C. Blais and D. G. Truhlar, J. Chem. Phys. **83**, 2201 (1985).
[5] N. C. Blais and D. G. Truhlar, Chem. Phys. Lett. **162(6)**, 503 (1989).
[6] F. J. Aoiz, V. J. Herrero, and V. Sáez, Chem. Phys. Lett. **161(3)**, 270 (1989).
[7] F. J. Aoiz, V. Candela, V. J. Herrero, and V. Sáez Rábanos, Chem. Phys. Lett. **169(3)**, 243 (1990).
[8] F. J. Aoiz, V. J. Herrero, and V. Sáez Rábanos, J. Chem. Phys. **95**, 7767 (1991).
[9] F. J. Aoiz, V. J. Herrero, and V. Sáez Rábanos, J. Chem. Phys. **94(12)**, 7991 (1991).
[10] F. J. Aoiz, V. J. Herrero, O. Puentedura, and V. Sáez Rábanos, Chem. Phys. Lett. **198(3,4)**, 321 (1992).
[11] F. J. Aoiz, V. J. Herrero, and V. Sáez Rábanos, J. Chem. Phys. **97**, 7423 (1992).
[12] F. J. Aoiz, L. Bañares, M. J. D'Mello, V. J. Herrero, V. Sáez Rábanos, L. Schnieder, and R. E. Wyatt, J. Chem. Phys. **101**, 5781 (1994).
[13] F. J. Aoiz, V. J. Herrero, O. Puentedura, and V. Sáez Rábanos, J. Chem. Phys. **100**, 758 (1994).
[14] F. J. Aoiz, H. K. Buchenau, V. J. Herrero, and V. Sáez Rábanos, J. Chem. Phys. **100**, 2789 (1994).
[15] L. Schnieder, K. Seekamp-Rahn, J. Borkowski, E. Wrede, K. H. Welge, F. J. Aoiz, L. Bañares, M. J. D'Mello, V. J. Herrero, V. Sáez Rábanos, and R. E. Wyatt, Science **269**, 207 (1995).
[16] F. J. Aoiz, L. Bañares, T. Díez-Rojo, V. J. Herrero, and V. Sáez Rábanos, J. Phys. Chem. **100**, 4071 (1996).
[17] F. J. Aoiz, L. Bañares, and V. J. Herrero, J. Chem. Phys. **105**, 6086 (1996).
[18] F. J. Aoiz, L. Bañares, V. J. Herrero, V. Sáez Rábanos, and I. Tanarro, J. Phys. Chem. A **101(35)**, 6165 (1997).
[19] E. Wrede, L. Schnieder, K. H. Welge, F. J. Aoiz, L. Bañares, V. J. Herrero, B. Martinez-Haya, and V. Sáez Rábanos, J. Chem. Phys. **106**, 7862 (1997).
[20] L. Bañares, F. J. Aoiz, V. J. Herrero, M. J. D'Mello, B. Niederjohann, K. Seekamp-Rahn, E. Wrede, and L. Schnieder, J. Chem. Phys. **108**, 6160 (1998).
[21] J. Z. H. Zhang and W. H. Miller, Chem. Phys. Lett. **153(6)**, 465 (1988).
[22] J. Z. H. Zhang and W. H. Miller, J. Chem. Phys. **91**, 1528 (1989).
[23] B. Lepetit and A. Kuppermann, Chem. Phys. Lett. **166**, 581 (1990).
[24] Y.-S. M. Wu, A. Kuppermann, and B. Lepetit, Chem. Phys. Lett. **186(4,5)**, 319 (1991).
[25] W. H. Miller and J. Z. H. Zhang, J. Phys. Chem. **95**, 12 (1991).
[26] M. J. D'Mello, D. E. Manolopoulos, and R. E. Wyatt, J. Chem. Phys. **94**, 5985 (1991).
[27] Y.-S. M. Wu and A. Kuppermann, Chem. Phys. Lett. **201(1–4)**, 178 (1993).
[28] Y.-S. M. Wu and A. Kuppermann, Chem. Phys. Lett. **235**, 105 (1995).
[29] A. Kuppermann, ''The Geometric Phase in Reaction Dynamics,'' in *Dynamics of Molecules and Chemical Reactions*, edited by R. E. Wyatt and J. Z. H. Zhang (Marcel Dekker, New York, 1996).
[30] M. P. de Miranda, D. C. Clary, J. F. Castillo, and D. E. Manolopoulos, J. Chem. Phys. **108**, 3142 (1998).
[31] A. Kuppermann, Faraday Discuss. **110**, 212 (1998).
[32] A. Kuppermann, Faraday Discuss. **110**, 217 (1998).
[33] E. E. Marinero, C. T. Rettner, and R. N. Zare, J. Chem. Phys. **80**, 4142 (1984).
[34] R. S. Blake, K.-D. Rinnen, D. A. V. Kliner, and R. N. Zare, Chem. Phys. Lett. **153(5)**, 365 (1988).
[35] K.-D. Rinnen, D. A. V. Kliner, R. S. Blake, and R. N. Zare, Chem. Phys. Lett. **153(5)**, 371 (1988).
[36] K.-D. Rinnen, D. A. V. Kliner, and R. N. Zare, J. Chem. Phys. **91**, 7514 (1989).
[37] D. A. V. Kliner, K.-D. Rinnen, and R. N. Zare, Chem. Phys. Lett. **166(2)**, 107 (1990).
[38] D. A. V. Kliner and R. N. Zare, J. Chem. Phys. **92**, 2107 (1990).
[39] D. E. Adelman, N. E. Shafer, D. A. V. Kliner, and R. N. Zare, J. Chem. Phys. **97**, 7323 (1992).
[40] D. Neuhauser, R. S. Judson, D. J. Kouri, D. E. Adelman, N. E. Shafer, D. A. V. Kliner, and R. N. Zare, Science **257**, 519 (1992).
[41] D. E. Adelman, H. Xu, and R. N. Zare, Chem. Phys. Lett. **203(5,6)**, 573 (1993).
[42] D. A. V. Kliner, D. E. Adelman, and R. N. Zare, J. Chem. Phys. **94**, 1069 (1991).
[43] D. P. Gerrity and J. J. Valentini, J. Chem. Phys. **79**, 5202 (1983).
[44] D. P. Gerrity and J. J. Valentini, J. Chem. Phys. **81**, 1298 (1984).
[45] D. P. Gerrity and J. J. Valentini, J. Chem. Phys. **83**, 2207 (1985).
[46] D. K. Veirs, G. M. Rosenblatt, and J. J. Valentini, J. Chem. Phys. **83**, 1605 (1985).
[47] D. P. Gerrity and J. J. Valentini, J. Chem. Phys. **82**, 1323 (1985).
[48] J.-C. Nieh and J. J. Valentini, Phys. Rev. Lett. **60(6)**, 519 (1988).
[49] H. B. Levene, D. L. Phillips, J.-C. Nieh, D. P. Gerrity, and J. J. Valentini, Chem. Phys. Lett. **143(4)**, 317 (1988).
[50] D. L. Phillips, H. B. Levene, and J. J. Valentini, J. Chem. Phys. **90**, 1600 (1989).
[51] J.-C. Nieh and J. J. Valentini, J. Chem. Phys. **92**, 1083 (1990).
[52] D. V. Lanzisera and J. J. Valentini, J. Chem. Phys. **103**, 607 (1995).
[53] R. Götting, H. R. Mayne, and J. P. Toennies, J. Chem. Phys. **80**, 2230 (1984).
[54] R. Götting, H. R. Mayne, and J. P. Toennies, J. Chem. Phys. **85**, 6396 (1986).
[55] S. A. Buntin, C. F. Giese, and W. R. Gentry, J. Chem. Phys. **87**, 1443 (1987).
[56] R. E. Continetti, B. A. Balko, and Y. T. Lee, J. Chem. Phys. **93**, 5719 (1990).
[57] T. N. Kitsopoulos, M. A. Buntine, D. P. Baldwin, R. N. Zare, and D. W. Chandler, Science **260**, 1605 (1993).
[58] N. E. Shafer, H. Xu, R. P. Tuckett, M. Springer, and R. N. Zare, J. Phys. Chem. **98**, 3369 (1994).
[59] F. Merkt and R. N. Zare, J. Chem. Phys. **101**, 3495 (1994).
[60] F. Merkt, H. Xu, and R. N. Zare, J. Chem. Phys. **104**, 950 (1996).
[61] H. Xu, N. E. Shafer-Ray, F. Merkt, D. J. Hughes, M. Springer, R. P. Tuckett, and R. N. Zare, J. Chem. Phys. **103**, 5157 (1995).
[62] L. Schnieder, K. Seekamp-Rahn, E. Wrede, and K. H. Welge, J. Chem. Phys. **107**, 6175 (1997).
[63] E. Wrede and L. Schnieder, J. Chem. Phys. **107**, 786 (1997).
[64] E. Wrede, L. Schnieder, K. H. Welge, L. Bañares, and V. J. Herrero, Chem. Phys. Lett. **265**, 129 (1997).
[65] N. E. Shafer, A. J. Orr-Ewing, W. R. Simpson, H. Xu, and R. N. Zare, Chem. Phys. Lett. **212(1,2)**, 155 (1993).
[66] N. E. Shafer-Ray, A. J. Orr-Ewing, and R. N. Zare, J. Phys. Chem. **99**, 7591 (1995).
[67] R. N. Zare and D. R. Herschbach, Proc. IEEE **51**, 173 (1963).
[68] J. Park, N. Shafer, and R. Bersohn, J. Chem. Phys. **91**, 7861 (1989).
[69] J. I. Cline, C. A. Taatjes, and S. R. Leone, J. Chem. Phys. **93**, 6543 (1990).

[70] C. A. Taatjes, J. I. Cline, and S. R. Leone, J. Chem. Phys. **93**, 6554 (1990).
[71] W. B. Chapman, M. J. Weida, and D. J. Nesbitt, J. Chem. Phys. **106**, 2248 (1997).
[72] M. Brouard, S. P. Duxon, P. A. Enríquez, and J. P. Simons, J. Chem. Soc., Faraday Trans. **89**, 1435 (1993).
[73] H. L. Kim, M. A. Wickramaaratchi, X. Zheng, and G. E. Hall, J. Chem. Phys. **101**, 2033 (1994).
[74] A. J. Alexander, F. J. Aoiz, L. Bañares, M. Brouard, J. Short, and J. P. Simons, J. Phys. Chem. A **101**, 7544 (1997).
[75] M. Brouard, D. W. Hughes, K. S. Kalogerakis, and J. P. Simons, J. Phys. Chem. A **102**, 9559 (1998).
[76] W. R. Simpson, A. J. Orr-Ewing, T. P. Rakitzis, S. A. Kandel, and R. N. Zare, J. Chem. Phys. **103**, 7299 (1995).
[77] W. R. Simpson, A. J. Orr-Ewing, and R. N. Zare, Chem. Phys. Lett. **212(1,2)**, 163 (1993).
[78] W. R. Simpson, T. P. Rakitzis, S. A. Kandel, T. Lev-On, and R. N. Zare, J. Phys. Chem. **100**, 7938 (1996).
[79] A. J. Orr-Ewing, W. R. Simpson, T. P. Rakitzis, S. A. Kandel, and R. N. Zare, J. Chem. Phys. **106**, 5961 (1997).
[80] S. A. Kandel, T. P. Rakitzis, T. Lev-On, and R. N. Zare, J. Chem. Phys. **105**, 7550 (1996).
[81] S. A. Kandel, T. P. Rakitzis, T. Lev-On, and R. N. Zare, Chem. Phys. Lett. **265**, 121 (1996).
[82] T. P. Rakitzis, S. A. Kandel, T. Lev-On, and R. N. Zare, J. Chem. Phys. **107**, 9392 (1997).
[83] S. A. Kandel, T. P. Rakitzis, T. Lev-On, and R. N. Zare, J. Phys. Chem. A **102**, 2270 (1998).
[84] W. C. Wiley and I. H. McLaren, Rev. Sci. Instrum. **26(12)**, 1150 (1955).
[85] D. A. Dahl, SIMION 3D version 6.0 (U.S. Department of Energy, Office of Energy Research, Idaho Falls, ID, 1995).
[86] E. E. Marinero, R. Vasudev, and R. N. Zare, J. Chem. Phys. **78**, 692 (1983).
[87] K.-D. Rinnen, D. A. V. Kliner, R. N. Zare, and W. M. Huo, Isr. J. Chem. **29**, 369 (1989).
[88] W. M. Huo, K.-D. Rinnen, and R. N. Zare, J. Chem. Phys. **95**, 205 (1991).
[89] K.-D. Rinnen, M. A. Buntine, D. A. V. Kliner, R. N. Zare, and W. M. Huo, J. Chem. Phys. **95**, 214 (1991).
[90] A. J. Heck, W. M. Huo, R. N. Zare, and D. W. Chandler, J. Mol. Spectrosc. **173**, 452 (1995).
[91] W. H. Press, B. P. Flannery, S. A. Teukolsky, and W. T. Vetterlich, *Numerical Recipes in Fortran* (Cambridge University Press, Cambridge, 1986).
[92] B. J. Huebert and R. M. Martin, J. Phys. Chem. **72**, 3046 (1968).
[93] Z. Xu, B. Koplitz, and C. Wittig, J. Phys. Chem. **92**, 5518 (1988).
[94] T. Kinugawa and T. Arikawa, J. Chem. Phys. **96**, 4801 (1992).
[95] P. M. Regan, S. R. Langford, A. J. Orr-Ewing, and M. N. R. Ashfold, J. Chem. Phys. **110**, 281 (1999).
[96] W. R. Simpson, Ph.D. Thesis, Stanford University, 1994.
[97] D. A. V. Kliner, K.-D. Rinnen, M. A. Buntine, D. A. Adelman, and R. N. Zare, J. Chem. Phys. **95**, 1663 (1991).
[98] P. M. Aker and J. J. Valentini, J. Phys. Chem. **97**, 2078 (1993).
[99] P. M. Aker, G. J. Germann, and J. J. Valentini, J. Chem. Phys. **96**, 2756 (1992).
[100] P. M. Aker, G. J. Germann, and J. J. Valentini, J. Chem. Phys. **90**, 4795 (1989).
[101] C. E. Moore, *Atomic Energy Levels* (National Bureau of Standards, Washington, 1971).
[102] R. Callaghan and R. J. Gordon, J. Chem. Phys. **93**, 4624 (1990).
[103] W. J. van der Zande, R. Zhang, R. N. Zare, K. G. McKendrick, and J. J. Valentini, J. Phys. Chem. **95**, 8205 (1991).
[104] W. J. van der Zande, R. Zhang, and R. N. Zare, in *Spectral Line Shapes*, edited by L. Frommhold and J. W. Keto (AIP, New York, 1990), Vol. 6, pp. 301–310.
[105] F. J. Aoiz, M. Brouard, P. A. Enríquez, and R. Sayos, J. Chem. Soc., Faraday Trans. **89**, 1427 (1993).
[106] G. M. McClelland, K. L. Saenger, J. J. Valentini, and D. R. Herschbach, J. Phys. Chem. **83**, 947 (1979).
[107] S. DePaul, D. Pullman, and B. Friedrich, J. Phys. Chem. **97**, 2167 (1993).